Extreme Mechanics Letters 4 (2015) 162–174

Contents lists available at ScienceDirect

Extreme Mechanics Letters

journal homepage: www.elsevier.com/locate/eml

What is the mechanism behind biological ferroelectricity?

Matthew Zelisko [a], Jiangyu Li [b], Pradeep Sharma [a,*]

[a] Department of Mechanical Engineering, University of Houston, Houston, TX 77004, United States
[b] Department of Mechanical Engineering, University of Washington, Seattle, WA 98195, United States

ARTICLE INFO

Article history:
Received 13 March 2015
Received in revised form 3 July 2015
Accepted 6 July 2015
Available online 11 July 2015

Keywords:
Elastin
Tropoelastin
Molecular dynamics
Piezoelectricity
Ferroelectricity

ABSTRACT

Biological tissues are soft, amorphous and often appear to possess a high degree of material symmetry. This would appear to preclude a phenomenon like ferroelectricity which, in the world of hard materials, only occurs in selected crystalline materials that are non-centrosymmetric. Recent experiments, however, indicate the presence of ferroelectricity in soft biological entities such as the protein elastin—a large biopolymer found in the extracellular domains of most tissues. In this letter, we present a model and an explanation for this intriguing observation. Based on a very simple physical hypothesis, we develop an analytical statistical mechanics model that, coupled with insights from molecular dynamics, provides a plausible mechanism underpinning biological ferroelectricity. Furthermore, we predict for the first time, piezoelectric properties of tropoelastin, a precursor/monomer of elastin—properties that are not easily obtained from experiments. Specifically we find that the piezoelectric constant of tropoelastin is larger than any known polymer.
© 2015 Elsevier Ltd. All rights reserved.

1. Introduction

The presence of electromechanical coupling in biological materials and its physiological significance has been an active area of research over the last several decades. Piezoelectricity was first discovered in bone samples in 1957 [1]. Shortly after that, in 1966, the pyroelectric phenomenon was also discovered in bones [2]. However, ferroelectricity, the rarest electromechanical coupling, was not observed in biological materials until 2012 when it was shown that the tissue from porcine aortic walls does indeed exhibit all the tell-tale signatures of ferroelectricity typically associated with hard ceramics like Barium Titanate or Lead Zirconium Titanate [3]. The main component of these tissue samples is a protein called elastin.

Elastin is found throughout various connective tissues. Aptly named, elastin is responsible for the elastic response of tissues, allowing the tissues and the relevant organs to retain their original shape after loading [4]. Elastin proteins are in fact long polymers composed of many monomer proteins called tropoelastin. While we typically think of monomers as small molecular units, a single human tropoelastin protein consists of up to 792 amino acids, or roughly 10,000 atoms [5]. The form most commonly used in experiments, and here for comparison, is a recombinant form of tropoelastin which is composed of 698 amino acids (isoform SHELd26A) or about 8,700 atoms [3,6,7].

Despite the discovery of ferroelectricity in biological materials, its physiological role is still somewhat unclear although there are several speculations regarding its significance. There is a large amount of elastin present in arteries, so one proposed possibility is that ferroelectric switching may limit the shear stress due to pulsatile flow [8]. Another notion that has been advanced is that the dipole switching associated with ferroelectricity may provide some type of memory function for our tissues and organs to retain their original shape. Either way, we feel that it is unlikely that the occurrence of this phenomenon is purely coincidental. Indeed, somewhat tentatively, the experimental results show that biological ferroelectricity

* Corresponding author.
E-mail address: psharma@uh.edu (P. Sharma).

http://dx.doi.org/10.1016/j.eml.2015.07.001
2352-4316/© 2015 Elsevier Ltd. All rights reserved.

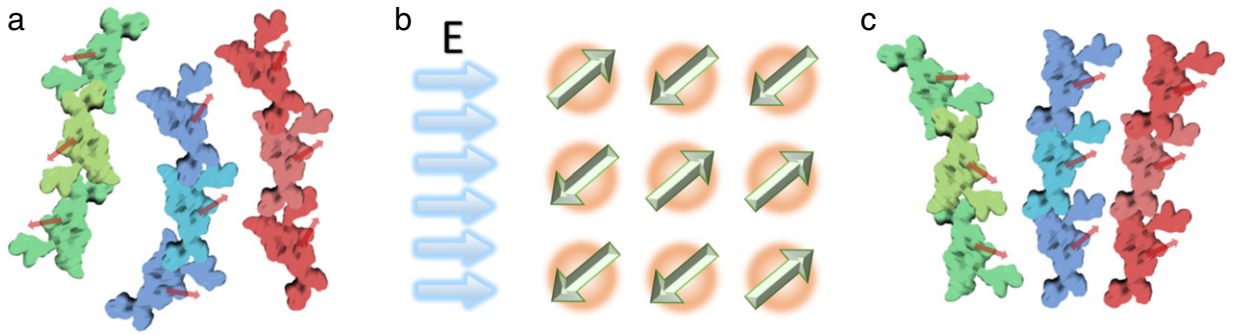

Fig. 1. (a) Two dimensional representation of amorphous elastin. Separate elastin polymers are shown in different colors, and shading is used to differentiate between tropoelastin monomers. The dipole moment associated with each monomer is shown by the red arrow. (b) Illustration of the two dimensional 2 site statistical mechanics model with general θ. Notice that $\phi_1 = 0$ and $\phi_2 = \frac{\pi}{2}$ are used as the angles made between a vector connecting two adjoining dipoles and the applied electric field. (c) Mostly aligned dipoles and monomers after/during application of an electric field sufficient for switching. (For interpretation of the references to color in this figure legend, the reader is referred to the web version of this article.)

in elastin is possibly linked to the aging process [9]. As our bodies age, elastin undergoes the slow process of glycation, i.e. the spontaneous, unassisted bonding of glucose to a protein. Once the concentrations of glucose bonded to elastin proteins are sufficiently high, such as during old age or in diabetics, elastin begins to degrade which may cause results such as lowered elastic response. This loss of elasticity can be easily viewed as wrinkles in the skin [10,11]. Coinciding with the change of mechanical properties, the ferroelectric response of elastin is also suppressed by the increasing severity of glycation [9]. Much research has been done on advanced glycation end-products (AGE), but none have focused on the effect of AGE on ferroelectricity [12,13]. The reason for the loss of ferroelectricity is again unknown, but as a first step, a reasonable starting point would be to first establish the mechanism underpinning biological ferroelectricity—this is the main goal of the current letter.

2. Hypothesis and central idea

Inspired from ideas already explored in the context of semi-crystalline polymers such as polyvinylidene fluoride (PVDF) [14], we propose the following picture of the likely mechanism for ferroelectricity in proteins like tropoelastin. We consider elastin as consisting of an amorphous array, or matrix, of tropoelastin monomers—each of which possesses a dipole moment. Alternatively, we could say that elastin is represented by a set of frozen dipoles which thermally fluctuate about some equilibrium angle. When subjected to an external electric field, the dipoles undergo some rotation and attempt to align with the field (Fig. 1). Ferroelectric switching, as will be elucidated in later sections, emerges as a cooperative effect. The overview of our modeling approach is as follows: (i) the statistical mechanics model of fluctuating frozen dipoles is adapted for the present case; (ii) molecular dynamics is used to estimate quantities like the monomer dipole moment (which feeds into the statistical mechanics model) and (iii) experimental observations are used to estimate the coercive field.

A comparison of the model with experimental observations provides reasonable assurance that our model and proposed mechanism is plausible. Furthermore, based on this model, we present numerical predictions of untested properties of tropoelastin—such as piezoelectric coefficient.

3. Biological ferroelectricity model

In the following (Section 3.1) we first present the statistical mechanics model that translates the physical picture of the preceding section into a simple analytical model. Molecular dynamics calculations, that connect with the analytical model, are presented in Section 3.2 and in subsequent subsections, we explore their implications (3.3 and 3.4).

3.1. Statistical mechanics framework

The model followed here was originally proposed by Broadhurst and Davis for PVDF [14]. They assume that the material is a collection of dipoles that thermally fluctuate; the dipoles interact only with the applied electric field, and the dipole–dipole interactions are purposefully neglected. In the general case, a dipole will have a probability, f_i, of being found in a preferred orientation specified by θ_i which is the angle between the applied electric field, E and the dipole orientation.

We start with the Helmholtz free energy of the system. While elastin is not crystalline, or even semi-crystalline, we approximate it as an evenly spaced set of dipoles allowing the use of terms such as the lattice energy of the crystal given by:

$$-U_0 \sum_{i=1}^{n} f_i^2 \tag{1}$$

where U_0 is the difference in energy between a filled lattice site and an empty site, and n is the number of preferred orientations in the "crystal". Here U_0 may be thought of as a material property which governs the ability of dipoles to change orientations. Our subsequent molecular dynamics results indicate that this scenario, even thought idealized, is a reasonable approximation (and price to pay) for analytical results. In the case of a two-site or two-orientation model, the system can be solved analytically.

This is tantamount to assuming that dipoles can only be up or down. One may assume a larger set of possible orientations and then the calculations must proceed numerically. We discuss this further in Section 3.4. The dipole–electric field interaction energy is then given by:

$$-m_0 E \sum_{i=1}^{n} f_i \cos\theta_i. \tag{2}$$

Here, m_0 is the average dipole moment of a single monomer. Next is the entropic contribution:

$$-k_b T \sum_{i=1}^{n} f_i \ln f_i. \tag{3}$$

The dipole–dipole interaction is somewhat more complex and requires an extra summation—this is omitted in the original model of Broadhurst and Davis [14].

$$\begin{aligned} E_{d-d} = \frac{m_0^2}{r^3} \sum_{i=1}^{n} \Bigg(& f_i^2 [2 - 3\{\cos^2(\theta_i - \phi_1) \\ & + \cos^2(\theta_i - \phi_2)\}] + f_i \sum_{j=1, j\neq i}^{n} f_j [2\cos(\theta_i - \theta j) \\ & - 3\{\cos(\theta_i - \phi_1)\cos(\theta_j - \phi_1) \\ & + \cos(\theta_i - \phi_2)\cos(\theta_j - \phi_2)\}] \Bigg). \end{aligned} \tag{4}$$

The mean separation of the dipoles is assumed to be a constant value, r. The angles ϕ_1 and ϕ_2 are defined as the angle between the electric field and a line connecting two interacting, nearest-neighbor dipoles. For simplification, we write these for the two dimensional case as $\phi_1 = \phi$ and $\phi_2 = \phi + \frac{\pi}{4}$. Later, the assumption will be made that $\phi = 0$.

Each of the energetic terms can be combined to yield the Helmholtz free energy (after duly subtracting the entropic contribution). Here A_0, the free energy when all f_i are equal, is used as the reference energy.

$$\begin{aligned} A_i - A_0 = & -U_0 \sum_{i=1}^{n} f_i^2 - m_0 E \sum_{i=1}^{n} f_i \cos\theta_i \\ & + k_b T \sum_{i=1}^{n} f_i \ln f_i + E_{d-d} - A_0. \end{aligned} \tag{5}$$

Appealing to the second law of thermodynamics, we minimize the free-energy subject to the constraint that $\Sigma f_i = 1$. Using λ to denote the Lagrange multiplier, the system of equations to solve is then given by:

$$\frac{\partial (A_i - A_0)}{\partial f_k} - \lambda \frac{\partial \Sigma f_i}{\partial f_k} = 0. \tag{6}$$

The model therefore represents a system of n nonlinear algebraic equations and can be solved for any number of preferred orientations or "sites". The complexity of the model is well-evident when the dipole–dipole interactions are added.

In the following, as a first approximation, we assume a 2-site model, i.e. dipoles can point up or down only. With this assumption, the set of equations given in (6) can be solved analytically. These orientations, with respect to the applied electric field E, will be evenly spaced and separated by an angle of π between the two, represented by $\theta_1 = \theta$ and $\theta_2 = \theta + \pi$. This is depicted in Fig. 1(b) for an arbitrary value of θ.

Equivalent to solving the set of equations given in (6), for a two-site model, Eq. (5) may be minimized directly. Prior to performing the minimization, we explore the form of the free energy by expanding the summations in (5) and substituting for θ_i and ϕ_i when $\theta = \phi = 0$. The Helmholtz free energy simplifies to

$$\begin{aligned} (A_i - A_0) = & -U_0(f_1^2 + f_2^2) - m_0 E \cos\theta (f_1 - f_2) \\ & + k_b T (f_1 \ln f_1 + f_2 \ln f_2) + \frac{m_0^2}{r^3}(2 f_1 f_2 \\ & - f_1^2 - f_2^2) - A_0. \end{aligned} \tag{7}$$

We note the following relationship between the magnitude of the apparent dipole moment, m, and the magnitude of the average dipole moment, m_0 based on the probabilities f_i and the incidental angles θ_i:

$$m\cos\theta = m_0(f_1 \cos\theta_1 + f_2 \cos\theta_2). \tag{8}$$

Substituting for θ_1 and θ_2, this relationship simplifies to

$$\frac{m}{m_0} = f_1 - f_2. \tag{9}$$

The ratio of m to m_0 may be thought of as the degree of polarization in the direction of the applied electric field. That is, when all of the dipoles are aligned with the electric field, $\frac{m}{m_0} = 1$, and when all of the dipoles are aligned against the electric field, $\frac{m}{m_0} = -1$, in the context of a positive applied electric field. All other orientations of dipoles will lie somewhere within this range. This can also be equated to the amount of polarization versus the total possible polarization and the actual polarization of the system can then be estimated by multiplying $\frac{m}{m_0}$ by $N * m_0$ where N is the number of dipoles included in the system. Using the relation in (9) along with the Helmholtz free energy given by Eq. (7) and the constraint that $f_1 + f_2 = 1$, we find the non-dimensional energy per dipole to be:

$$\begin{aligned} \frac{A_i - A_0}{k_b T} = & -\frac{1}{2}\frac{U_0}{k_b T}\left(\frac{m}{m_0}\right)^2 - \frac{m_0 E}{k_b T}\cos\theta\left(\frac{m}{m_0}\right) \\ & + \frac{1}{2}\Bigg[\left(1 + \frac{m}{m_0}\right)\ln\left(1 + \frac{m}{m_0}\right) \\ & + \left(1 - \frac{m}{m_0}\right)\ln\left(1 - \frac{m}{m_0}\right)\Bigg] \\ & - \frac{m_0^2}{r^3 k_b T}\left(\frac{m}{m_0}\right)^2. \end{aligned} \tag{10}$$

This results from setting $A_0 = A_i$ when A_0 is the disordered state and $f_1 = f_2 = \frac{1}{2}$. Eq. (10) is non-dimensional and illustrates the behavior of the free energy as a function of the electric field and the degree of polarization. The free energy is shown in as a function of electric field and degree of polarization in Fig. 2(a) and as a function of the degree of polarization only (although multiple values of the electric

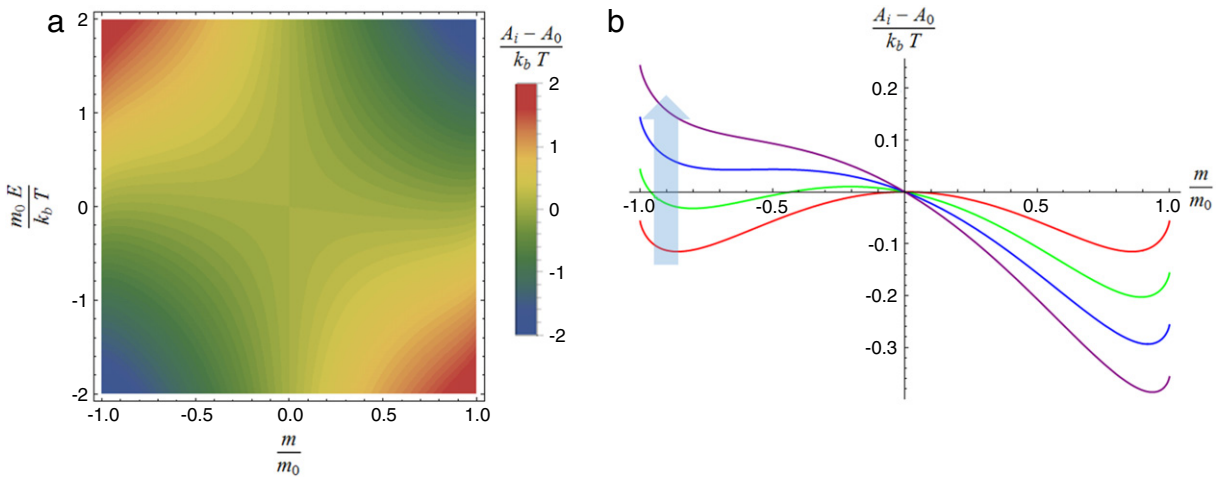

Fig. 2. Effect of the applied electric field on the free energy of the two-site model shown for arbitrary value of $\frac{U_0}{k_b T} + 2\frac{m_0^2}{r^3 k_b T}$. (a) Two dimensional contour plot of the free energy, minima and maxima are represented by blue and red respectively. (b) Free energy as a function of polarization, for selected values of applied electric field. These would be horizontal slices from the contour plot. The light blue arrow indicates which direction the free energy landscape "moves" towards as the electric field is increased. The red line shown is for zero applied electric field. (For interpretation of the references to color in this figure legend, the reader is referred to the web version of this article.)

field are illustrated) in Fig. 2(b). Fig. 2 is shown for an arbitrary value of the parameter $\frac{U_0}{k_b T} + 2\frac{m_0^2}{r^3 k_b T}$; we will derive the actual value for this parameter in Section 3.3. Now that the free energy of the two-site model is known, we may minimize the energy by taking the derivative with respect to $\frac{m}{m_0}$ and setting it equal to zero. This gives the relation relating the (non-dimensional) electric field to the degree of polarization as:

$$\frac{m_0 E}{k_b T}\cos\theta = -\frac{U_0}{k_b T}\left(\frac{m}{m_0}\right) + \frac{1}{2}\ln\left(\frac{1+\frac{m}{m_0}}{1-\frac{m}{m_0}}\right) - 2\frac{m_0^2}{r^3 k_b T}\left(\frac{m}{m_0}\right). \tag{11}$$

Alternatively, expanding the set of equations given by (6) along with the applied constraint gives a system of three equations for a two site model.

$$-2U_0 f_1 - m_0 E\cos\theta + k_b T(1+\ln f_1) + 2\frac{m_0^2}{r^3}(f_2 - f_1) - \lambda = 0 \tag{12}$$

$$-2U_0 f_2 + m_0 E\cos\theta + k_b T(1+\ln f_2) + 2\frac{m_0^2}{r^3}(f_1 - f_2) - \lambda = 0 \tag{13}$$

$$f_1 + f_2 = 1. \tag{14}$$

Solving these equations and using the relation given in (8)/(9) will lead to the exact same result as given by Eq. (11). There is a common parameter; $\frac{U_0}{k_b T} + 2\frac{m_0^2}{r^3 k_b T}$ that emerges in both Eqs. (10) and (11) that cannot be estimated without some additional information about the material which is being examined. Estimation of this parameter is discussed in the next two sections.

3.2. Molecular dynamics simulation results

There is no experimental information on the structure of tropoelastin, other than the sequence [6] and the general shape [7]. This is a major obstacle since the folded structure of this monomer is beyond the scope of molecular dynamics. We note here that we consider the 698 amino acid recombinant form of tropoelastin (SHELd26A) rather than the 792 amino acid form of human tropoelastin, in order to make a better comparison with the available experimental results. Accordingly, we first attempted to use the so-called homology modeling approach to determine the folded structure of the protein. Homology modeling takes the protein's amino acid sequence as input, then searches through existing (extensive) databases to find the best matches for common patterns in the sequence. A previously generated structure was found in the ModBase databank [15], but this structure showed almost no similarity to the experimentally determined general shape of Baldock et al. and only modeled approximately 80% of the protein's sequence [5].

Since a satisfactory homologous model does not exist for tropoelastin, we used the protein threading approach. Protein threading, also called fold recognition, uses the amino acid sequence to place each amino acid in the best fit position based on other folds commonly found in nature; this works because there are only around 1300 known folds to choose from [16]. Many remote servers are readily available to perform protein structure prediction based on this protein threading algorithm. Based on the results of several different servers, the structure predicted by the *SPARKS*^{X} server was used as an initial structure for tropoelastin which is, upon analysis, fairly close to the expected general (experimental) structure [17].

All molecular dynamics simulations were performed using GROMACS version 4.5.6, with the CHARMM36 force field and SPC/E explicit water model [18–23]. Several steps were taken to equilibrate the structure

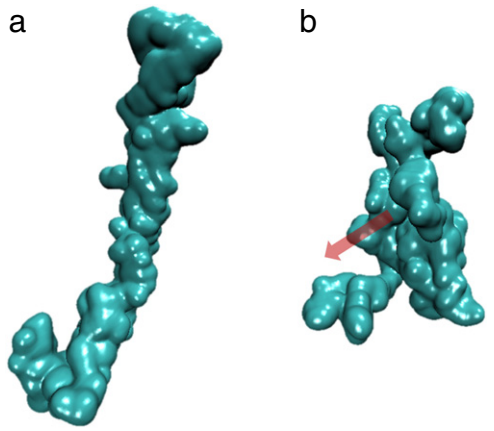

Fig. 3. Protein structures rendered using Visual Molecular Dynamics [24]. (a) Initial tropoelastin structure obtained from protein threading, after energy minimization, end-to-end length is 21.7 nm. (b) Structure after including the desmosine cross-link and equilibration, red arrow indicates the direction of the dipole moment. (For interpretation of the references to color in this figure legend, the reader is referred to the web version of this article.)

prior to performing any production molecular dynamics simulations. An energy minimization was first performed on the folded structure taken from the protein threading results using the conjugate gradient method until the largest remaining force was less than 10 kJ mol^{-1} nm^{-1}. The energy minimized structure has an end-to-end length of 21.7 nm, somewhat higher than the expected value of 16 nm [7]. The resulting structure for tropoelastin is shown in Fig. 3(a) [24]. After energy minimization, the system was solvated with water molecules; energy minimization was done on the solvated system and a molecular dynamics simulation was performed for 1000 ps to equilibrate the system. All molecular dynamics were performed using leapfrog integration with a time-step of 0.002 ps at 310 K and all bond lengths constrained.

Since we have only used the amino acid sequence of tropoelastin to predict the structure, only peptide bonds are present to create the backbone of the protein; there are no additional bonds between the amino acid side chains anywhere within the structure. This simplification of the structure leaves out some detail. In particular, tropoelastin is a highly cross-linked protein with both inter- and intramolecular cross-links present. For simulations of one monomer, we may ignore the intermolecular cross-links and only consider those that are intramolecular. Tropoelastin is composed of hydrophobic domains, classified as glycine or proline rich, alternating with lysine cross-linking domains, classified as KA for alanine rich of KP for proline rich [25]. Only one cross-linking domain has been highly studied in tropoelastin; that is intramolecular cross-linking which occurs between lysine residues in exons 19 and 25, both of which are alanine rich cross-linking domains. We may also note, that intermolecular cross-linking is believed to occur between exons 19 and 25 of one monomer with exon 10 of the linked monomer [26]. The sequence for each exon is provided with the lysine residues involved in the cross-linking in bold [7,25]:

Exon 19	GVVSPEAAAKAAA**K**AA**K**Y
Exon 25	GPGGVAAAA**K**SAA**K**VAAKAQL

This cross-link is approximated by adding a few simple bond potentials between the lysine side chain atoms involved with equivalent strengths to the other bonds provided by the force field. After adding the cross-linking, the structure is equilibrated for another 2000 ps and oriented along its principal axes to be used as a starting structure in the remainder of the simulations. The starting structure is shown in Fig. 3(b). The average end-to-end distance is found to be 12.7 nm with fluctuations as high as 15 nm, slightly lower than the experimental value of 16 nm [7].

Finally, a production molecular dynamics simulation is performed on the equilibrated structure for 1000 ps with the protein backbone atoms restrained to prevent unwanted free rotation of the monomer. From this, we obtain the radius of gyration (R_g), which has a mean value of 4.65 nm over the entire simulation, and the time averaged dipole moment of tropoelastin monomer is calculated to be 581 $\pm$ 33 D. The general direction of the dipole moment is superimposed on top of the tropoelastin structure in Fig. 3(b). The average volume of the molecule over this time is approximately 54.0 ± 0.23 nm^3; this leads to an overall polarization of 3.59 $\mu C\,cm^{-2}$. (The method for calculation of the volume is discussed in Section 4.1.) This is slightly higher than the experimental value found to be around 2 $\mu C\,cm^{-2}$ [27]. This discrepancy arises from the fact that we consider the polarization of a single monomer, while the experimental work considers the polarization of a bulk elastin sample. This bulk material, with several tropoelastin monomers, may have dipoles that are not perfectly aligned as well as additional volume from free space between monomers due to imperfect packing of the molecules. Therefore, it is expected that the value found for a single tropoelastin molecule would be higher.

3.3. The final model: putting it all together

Now that the dipole moment and radius of gyration of a tropoelastin monomer have been found, the only remaining data necessary for the model is the coercive electric field. The coercive field is the magnitude of the applied electric field at which ferroelectric switching occurs, and must be found from experiments. Detailed experiments, based on piezoelectric-force-microscopy (PFM) characterization, have been already presented by Li and co-workers [3,9,27]. Due to the asymmetry of the experimental data, the coercive field, based on the voltage bias applied during the PFM experiment and the sample size, was averaged between the negative and positive values to find a magnitude of approximately 10,300 $\frac{V}{m}$ [27]. This is the coercive field for a larger sample than only a single molecule, therefore when non-dimensionalizing the data we must use $m_0 * N$, where N is the number of dipoles in the system, in place of the dipole moment of a single monomer. We make this distinction here, but do not explicitly show this in the equations. Based on the details of the experiments [9,27], N is found by calculating the density of the tropoelastin, multiplying by the volume affected

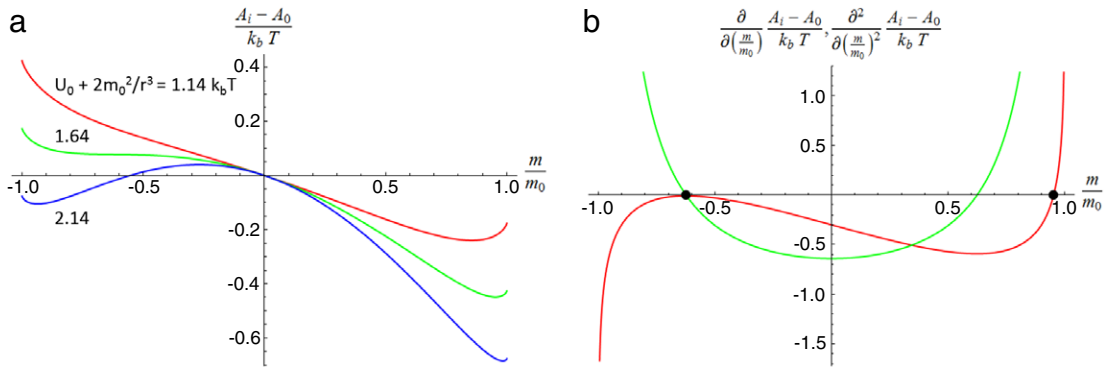

Fig. 4. (a) Free energy shown for different values of lattice energy parameter at the calculated critical field. (b) The first and second derivatives of the free energy, taken with respect to the degree of polarization, are shown by the red and green lines respectively. The black dots show when the first derivative is zero. (For interpretation of the references to color in this figure legend, the reader is referred to the web version of this article.)

by the PFM tip, and dividing by the mass of a single tropoelastin monomer (60,000 Da). The entire sample has a volume of 2.7 mm^3 with a mass of 70 μg yielding a density of 25.9 $\frac{\mu g}{mm^3}$. The size of the sample affected by the PFM tip is estimated as a hemisphere with radius of 50 nm for a volume of 261,799 nm^3. Multiplying the pertinent volume by the density of the sample and dividing by the mass of a single monomer, we find that the sample contains $N = 68$ tropoelastin monomers. This supports the previous statement that the monomers in the bulk sample are not perfectly packed and the sample will have some empty volume; simply dividing the affected volume by the volume of a single tropoelastin molecule would suggest many more monomers in the sample. Using this result we estimate the non-dimensional critical field to be $\left(\frac{m_0 E_c}{k_b T}\right)_{crit} = 0.33$.

The next step is to estimate $\frac{U_0}{k_b T} + 2\frac{m_0^2}{r^3 k_b T}$. Re-arranging the Helmholtz free-energy in Eq. (10), given that $\left(\frac{m_0 E_c}{k_b T}\right)_{crit}$ has been determined, and substituting the value of $\left(\frac{m_0 E_c}{k_b T}\right)_{crit}$, when $\theta = 0$, we find:

$$\frac{A_i - A_0}{k_b T} = -\frac{1}{2}\left(\frac{U_0}{k_b T} + 2\frac{m_0^2}{r^3 k_b T}\right)\left(\frac{m}{m_0}\right)^2 - 0.33\left(\frac{m}{m_0}\right) + \frac{1}{2}\left[\left(1 + \frac{m}{m_0}\right)\ln\left(1 + \frac{m}{m_0}\right) + \left(1 - \frac{m}{m_0}\right)\ln\left(1 - \frac{m}{m_0}\right)\right]. \quad (15)$$

Using the radius of gyration calculated from the molecular dynamics simulation where the mean value over 1 ns is found to be 4.65 nm, the mean spacing between dipoles, r can be estimated as $r = 2R_g = 9.3$ nm. This result combined with the dipole moment to find the dipole–dipole interaction contribution to the unknown parameter yields $2\frac{m_0^2}{r^3 k_b T} = 1.0 \times 10^{-5}$. We will show shortly that this term is negligible compared to $\frac{U_0}{k_b T}$. Eq. (15) is plotted for different values of $\frac{U_0}{k_b T} + 2\frac{m_0^2}{r^3 k_b T}$ in Fig. 4(a). For some of the cases, there exist two distinct free energy minima. These correspond to the two possible orientations of the dipoles. When two minima exist, the switching from one site to the other will note be complete—for the given electric field. Therefore the lattice energy is too high for the critical field. On the other hand, the case where there is only one distinct minimum indicates that the applied field has already caused complete switching. For the latter, the lattice energy is too low for the applied field. This leaves only the case where the free energy shows a minimum for one site, and a zero slope for the other. The system is then neutrally stable in one configuration, as it should be at the critical field, and the value for $\frac{U_0}{k_b T} + 2\frac{m_0^2}{r^3 k_b T}$ can estimated from this condition—which we find to be about 1.64. This is a very reasonable value given the following observation: for PVDF, Broadhurst and Davis estimated this value to be 3 (—their coercive field was much higher than ours) [14]. The ideal value is found by taking the first and second derivatives of (15) with respect to $\frac{m}{m_0}$ then finding where the first derivative is zero. For the case presented here, the first derivative must have two roots, and the second derivative must be zero at one of the roots. These equations were solved numerically, by iterating over different values of $\frac{U_0}{k_b T} + 2\frac{m_0^2}{r^3 k_b T}$ until the proper conditions were met. The derivatives for the selected value of 1.64 can be seen Fig. 4(b), which shows that the first derivative has two unique roots, and at these points the second derivative is zero for one root and positive for the other. This implies that one root is a minimum, while the other is neither a minimum nor maximum—precisely the condition we were looking for.

Based on the calculation done earlier, it is immediately clear that $\frac{U_0}{k_b T} \gg 2\frac{m_0^2}{r^3 k_b T}$; therefore we can essentially ignore the contribution of the dipole–dipole interactions. Here we will simply lump that small contribution in with the dominant term. Additionally, we know from the critical temperature (or what is essentially the same, the transition point between two and one minima in Fig. 4(a)) that a lower bound is 1.0, found by evaluating Eq. (10) at zero electric field. This can help us effectively find the Curie temperature for the model system. Since we know that $\frac{U_0}{k_b T} > 1.0$ for a ferroelectric response, inserting the estimated value for U_0, the Boltzmann constant, k_b, and solving then inequality leads to the estimation of the Curie temperature, $T_C = 508$ K. This is in good agreement with the experimental value of 470 K [27].

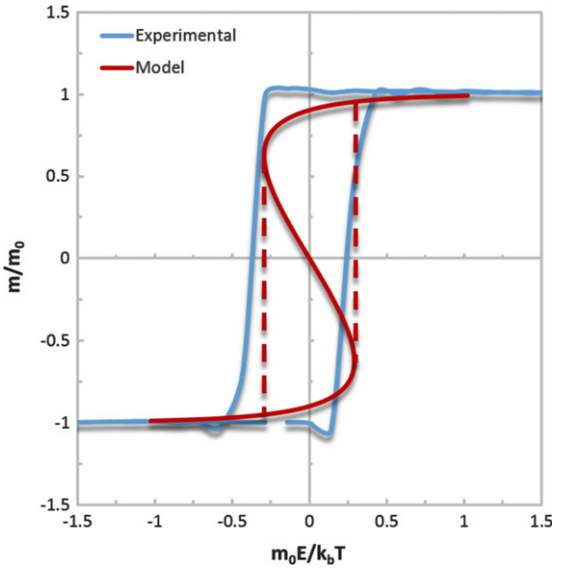

Fig. 5. Comparison of the experimental data [9] with the model represented by Eq. (11).

Fig. 5 shows the experimental data and the results of our model. The dotted lines in the hysteresis loop are a guide to the eye since our model simply "jumps" at those points of transition. The two-site model exhibits some unphysical behavior in the middle, which is an artifact of switching the independent and dependent variables when plotting (11). This is discussed further in the next section where we also present results from the six-site model. Additional insights, including the hysteresis prediction, are discussed in the context of a comparison between the 2-site and 6-site models.

3.4. Extension of the model to more than 2 sites

The two-site model is a simplification—albeit one that well-captures the essential physics. Its chief advantage, aside from the conceptual simplicity, is its analytical tractability. Physically, the dipoles will be able to align in almost any direction, not simply with or against the electric field. The set of equations represented by (6) may be solved for any number of sites; the two-site model was analytically solved in the preceding section but the inclusion of a higher number of sites requires a numerical solution.

However, "more sites" is not necessarily better. Simple physical considerations and symmetry arguments impose some restrictions on the number of sites that can be used in our modeling framework. First, the model must have sites that align with the applied electric field for complete ferroelectric switching to occur. Consider a model with three evenly spaced sites; the first aligns in the positive direction of the applied electric field and the other two make angles of $\pm\frac{2\pi}{3}$ with the first site. It is clear that if the electric field is positive, complete switching can occur, that is $f_1 \rightarrow 1$. However, if the electric field is applied in the negative direction, at an angle of π with respect to site one, complete switching will not occur. In that case, $f_2, f_3 \rightarrow 0.5$ and the maximum degree of polarization achieved would be $(-)\frac{1}{2}$; found from the equivalent to Eq. (8) with three sites.

The second restriction is that the model must have no sites aligned perpendicular to the applied electric field, as is the case of a four site model with the sites spaced evenly at angles of $\frac{\pi}{2}$. Sites 1 and 3 are aligned with the positive and negative electric fields respectively, but sites 2 and 4 are perpendicular to any applied electric field. Complete switching may occur based on the orientations of sites 1 and 3, however we cannot determine any information about how the applied electric field interacts with sites 2 and 4. The free energy contributions from the dipole–field interaction given by (2) shows that the energy depends on the cosine of the angle between the electric field and the dipole. When the dipoles are aligned at an angle of $\pm\frac{\pi}{2}$ with respect to the electric field, the dipole–field interaction energy goes to zero. Therefore the sites 2 and 4 can be thought of as neutrally stable sites that will not change regardless of the strength of the applied electric field—unless there is some perturbation that moves the dipole out of its equilibrium state. Due to this, solving the four site model, will yield the same result as the two site model since the additional sites do not interact with the external electric field.

In a large enough system, that has not been poled to bias the probability of finding dipoles in certain orientations, the dipoles will be evenly distributed. To satisfy this condition and avoid introducing any bias into the model, we should use sites that are evenly spaced. For evenly spaced models, we have already detailed why three and four sites will fail; a five site model will fail for the same reason as three sites. Therefore, beyond the 2-site model, the simplest one is a 6-site model. A 6-site model will not violate either of the restrictions mentioned above, but will lead to a system of 6 nonlinear equations (and 1 linear equation) that must be solved simultaneously.

Our initial attempts to implement a 6-site model were unsuccessful. Therefore, we outline here several subtleties in its implementation to facilitate replication of our work. First and foremost, the value of $\frac{U_0}{k_bT}$ used in the 2-site model should not be used in the 6-site model. Indeed, for the 6-site model $\frac{U_0}{k_bT}$ cannot be found analytically from Eq. (15). While the 2-site model requires $\frac{U_0}{k_bT} > 1.0$ to exhibit ferroelectric behavior, the requirement for the 6-site model is $\frac{U_0}{k_bT} > 1.9182$ [28]. Broadhurst and Davis suggest that a good approximation is $\frac{U_0}{k_bT} \approx 2 + (\frac{m_0E}{k_bT})_{critical}$. For the case described here this condition translates to $\frac{U_0}{k_bT} = 2.33$ for the 6-site model [14]. The Curie point for the 6-site model can be computed in the same manner as done for the 2-site model and yields $T_c = 377$ K—somewhat lower than that predicted experimentally.

As mentioned earlier, the 6-site model yields a system of 7 equations, 6 of which are nonlinear, and 7 unknowns. To find all possible solutions for the 6-site model the freely available OpenOpt optimization software was used [29]. The solver "interalg" was applied through the OpenOpt System of Non-Linear Equations (SNLE) algorithm. This solver is capable of finding all solutions to a set of nonlinear equations when the upper and lower bounds are the

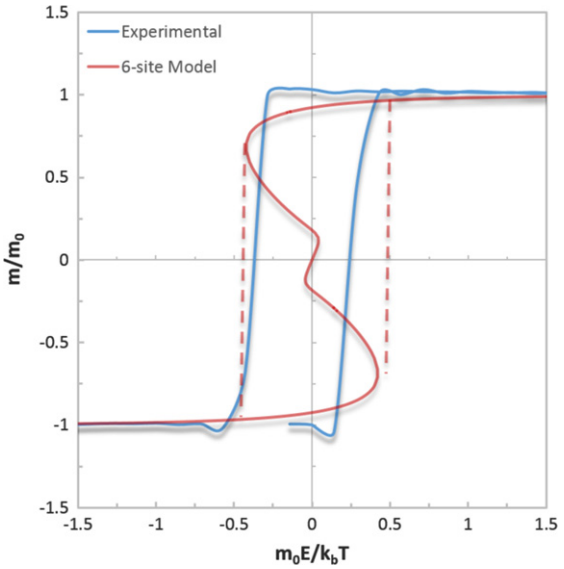

Fig. 6. Comparison of the experimental data [9] with the 6-site model, based on the set of equations given in (6).

solution are known. The numerical solution obtained for the 6-site model along with the experimental data is shown in Fig. 6. As evident, the 6-site model yields results that are both qualitatively and quantitatively quite similar to the 2-site model (Fig. 5). The dotted lines are added to show where a jump will occur. We note that the fit to the data is not quite as good as the two-site model; this is caused by the fact that $\frac{U_0}{k_bT}$ must be estimated for the 6-site model. This parameter could be adjusted to give a *fit* similar to that of the 2-site model (as done by Broadhurst and Davis) but we do not feel that it is necessary in the present case.

Up to this point, the models have been solved to show the relationship between the degree of polarization and the applied electric field. These results do suggest a hysteresis behavior, but to actually show that the model predicts the ferroelectric hysteresis an additional step must be undertaken. Using the origin as the starting point, the Newton–Raphson method is used to find the 6-site solutions. The initial solution is taken to be one where the probabilities of all sites are equal and the applied electric field is zero. From this solution, the electric field is increased by small increments and the Newton–Raphson method is used to predict the new solution. The electric field is then increased further and a new solution is found using the previous solution as the initial guess. This is repeated to map out the ferroelectric hysteresis loop as shown in Fig. 7(a) for the 2-site model and 7b for the 6-site model. We see that this method exhibits the unphysical solutions shown in Figs. 5 and 6, but once a "jump" is made to the outer curve the physically meaningful solution branches are followed and the unrealistic solutions are never revisited regardless of the repeated cycling of the electric field.

4. Origin of dipole moment and the switching process

The dipole moment of a single tropoelastin monomer is found earlier to be 581 D. This can be attributed to one dominating property of the monomer. We postulate that the high dipole moment is predominantly a result of the structure of the protein; this is due to the elongated, asymmetrical shape and the large mass of the molecule. We have mapped out the partial charges to create the set of 2-D surface plots shown in Fig. 8 for the tropoelastin molecule. From the surface plots it is clear that there is no distinct location which contains a large positive or negative charge. Rather, the partial charges are fairly evenly

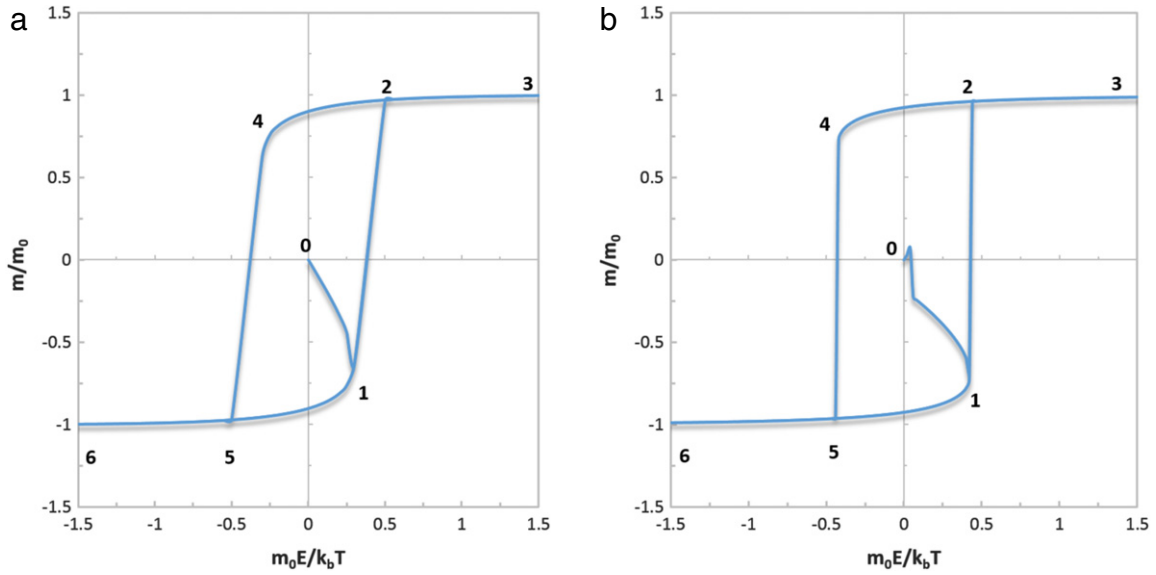

Fig. 7. The model solved for (a) 2-sites and (b) 6-sites. In both cases the model begins with a solution consisting of evenly spaced probabilities at the origin. As the electric field is increased, the solutions follow the path from points 0–1 to 2–3. Then after incrementally decreasing the electric field, the solutions flow from point 3–4 to 5–6. Upon cycling the electric field, the solutions always follow the points in order but never revisits point 0.

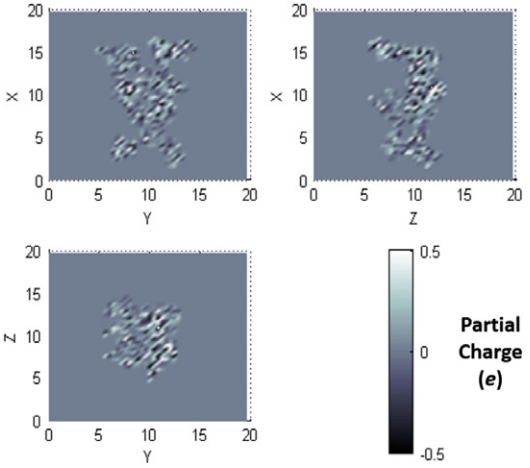

Fig. 8. 2-D surface plots illustrating the locations of the partial charges in a tropoelastin molecule. White indicates areas of positive charge, while black indicates negatively charged areas. Each plane in the Cartesian system is shown to give a complete picture.

distributed throughout the molecule. This observation is confirmed by calculating the locations of the positive and negative centers of charge. Over a 1 ns simulation, the mean separation between these two locations was found to be only 0.0114 ± 0.0005 nm. However, even with such a small distance separating the centers of charge, the overall size of the molecule (8694 atoms), with each atom assigned some partial charge as stated in the CHARMM force field, has many partial charges to consider. The sum of the positive partial charges in the tropoelastin monomer is $+992.85e$ while the sum of the negative charges is $-954.85e$. The total charge of the molecule, which is due to the inclusion of charged amino acids (predominantly lysine) in the protein structure, is $+38e$; this is the sum of the positive and negative partial charges for the entire molecule. Compounding the issue of many partial charges, we have a non-neutral molecule; therefore the dipole moment must be computed with respect to the center of mass leading to a rather large dipole moment despite the relatively close centers of charge.

4.1. Switching mechanism

In this section, we elaborate on the mechanism by which the ferroelectric switching occurs. There are three possible explanations for the switching. First, there could be a rearrangement of the tropoelastin protein's side chains; in this case the shape of the protein backbone would remain relatively intact and the charged atoms on the side chains would move to cause the dipole moment to change directions. The second explanation, could be that the entire tropoelastin molecule rotates to align the dipole moment with an applied electric field. Lastly, the tropoelastin molecule could experience a slight reconfiguration while the inter-molecular cross-linking residues remain "fixed" as if rigidly bound to other monomers. We believe that this final mechanism is the most likely mechanism for the dipole switching in elastin.

Simulations are performed for 1 ns in all cases with an applied electric field of 0.05 V nm^{-1} in the opposite direction of the highest component of the dipole moment. The average length of the simulation box across which the electric field applied is 20 nm, therefore the applied electric field is equivalent to a bias voltage of 1 V across the protein. The high applied electric field is to ensure that switching does occur on the timescales available to molecular dynamics. The first simulation is performed with position restraints applied to the backbone atoms while all other atoms are free to move. The second simulation is done with no restraints such that the entire protein may move, and the third case is performed with lysine cross-linking residues in exons 10, 19, and 25 restrained [7,26]. During the simulations the total dipole moment and its components are monitored versus time. At the start of all simulations, the strongest component of the dipole moment lies in the $-z$ direction and the electric field is applied in the $+z$ direction. When switching occurs, we expect to see a large change in the z component of the dipole moment.

Fig. 9 shows the dipole moments versus time for the first two simulations. When the backbone is held fixed, there is very little change in the dipole moment or its components as shown in Fig. 9(a). In this case,

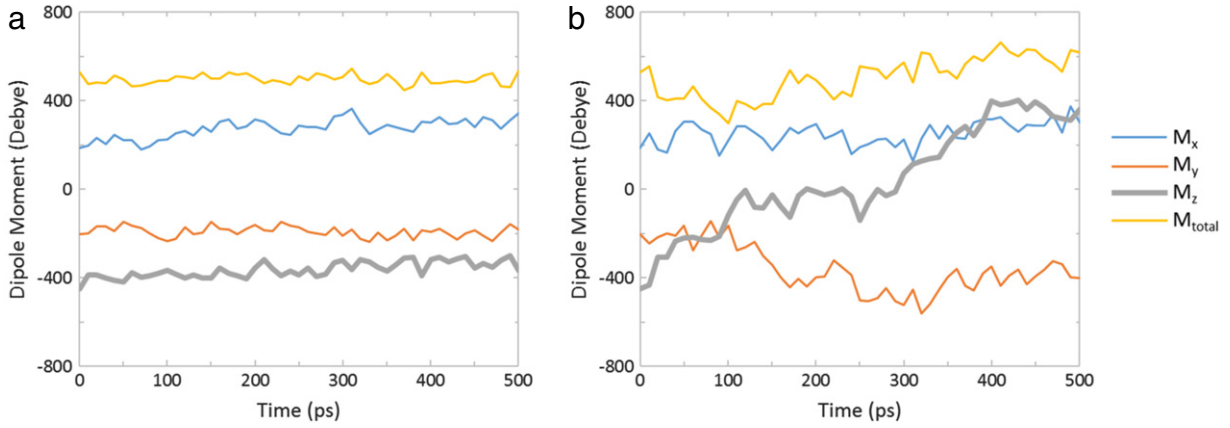

Fig. 9. Total Dipole Moment and components with applied electric field. The thick gray line indicates the "z" component, and the external field is applied opposite to its initial orientation. (a) The protein back bone is held fixed, while side chains are free. (b) The entire protein is free to move.

rearrangement of the amino acid side chains does not allow sufficient movement of the charged atoms to see a change in the dipole moment. For the second simulation, as shown by Fig. 9(b), a large change in the z-component occurs rather quickly, within the first 500 ps. Thus, in the second case switching has occurred. Tracking the positions of the atoms versus time shows that in this case the tropoelastin molecule undergoes an essentially rigid body rotation causing the switching to occur. No significant changes occurred to the dipole moments after the first 500 ps of simulation, so the data past that is omitted from Fig. 9.

The third possible mechanism is also tested and shows that switching of the dipole moment can occur while the cross-linking amino acids are held fixed. In this case some small amount of deformation, in the form of bending, occurs in the tropoelastin backbone. We believe that this is the most likely mechanism for the observed ferroelectric switching in elastin, and these results will be presented in more depth in a future publication. For the statistical mechanics model presented in Section 3.1, the exact mechanism is not as important as the fact that we have shown that tropoelastin monomers possess a dipole and that dipole will change direction under an electric field—thus verifying the assumptions made for the model. We propose that the mechanism responsible for the ferroelectric behavior in elastin is that each tropoelastin monomer possesses a large dipole moment, and when exposed to a sufficient electric field these monomers either rotate cooperatively and rigidly or undergo a slight bending deformation such that their dipole moment aligns as closely as possible with the electric field.

5. Piezoelectricity

One of the advantages of developing a quantitative model for biological ferroelectricity is that it allows prediction of properties that may not be easily estimated from experiments. Ferroelectric materials also possess both piezoelectric and pyroelectric properties. The pyroelectricity of elastin has been investigated experimentally [27], but the piezoelectric coefficient has largely been an afterthought with only the order of magnitude estimated [9]. Neither piezo- nor pyroelectric properties have been predicted for a single tropoelastin monomer due to the difficult nature of working with such small molecules experimentally where many traditional quantities, such as stress, are ill-defined. For example, just to find the Young's modulus of tropoelastin requires experimental data, theory, and some assumptions [7].

A material with frozen dipoles and/or space charges is referred to as a electret. A model for piezoelectricity in dipole electrets has already been derived [30]. This model was originally created for amorphous solids containing multiple partially aligned, frozen dipoles. Under an applied electric field, the dipoles in elastin will become aligned and essentially fixed (other than small thermal fluctuations), allowing us to extend this model to be used here. The important equation taken from this model can be written as

$$\frac{\partial P}{\partial p} = -P\left[\frac{1}{V}\frac{\partial V}{\partial p}\left(1+\frac{\epsilon-1}{3}-(\epsilon+2)\frac{D}{V^2}\right) + \frac{J_1(\phi_0)}{J_0(\phi_0)}\frac{\partial \phi_0}{\partial p}\right] \tag{16}$$

where p is pressure and ϵ is the relative permittivity of the material. The constant D is related to electrostriction and we will assume that this term is small enough to be neglected (since the relative permittivity changes very little with volume). The last term contains two Bessel functions J_0 and J_1, and ϕ_0 is the amplitude with which the dipole oscillates around its equilibrium position. In the case of constant temperature, the last term is also small enough to be neglected. Lastly, P is the spontaneous polarization in the material, given by:

$$P = \left(\frac{N}{V}\right)\langle m\rangle. \tag{17}$$

Here N is the number of dipoles in the system; this will be set to 1 for a single tropoelastin monomer here. We note here that Eq. (17) essentially equates to the value that was used for m_0 in the statistical mechanics model presented earlier divided by the volume of the tropoelastin molecule. We also note that the first term in the bracket is the compressibility of the material

$$\beta = -\frac{1}{V}\frac{\partial V}{\partial p}. \tag{18}$$

Substituting this relation and removing the negligible terms from Eq. (16) leaves us with:

$$\frac{\partial P}{\partial p} = \frac{m_0}{V}\left[\beta\left(1+\frac{\epsilon-1}{3}\right)\right] \tag{19}$$

where m_0 is already known, and ϵ, β, and V can be found from molecular dynamics. The results for these quantities, and all other important results and values for the following sections, are reported in Table 1.

Table 1
Summary of properties used in Eqs. (19)–(21).

Property	Value
k_b [a]	1.38×10^{-23} N m K^{-1}
T [a]	310 K
ϵ_0 [a]	8.85×10^{-12} A^2 s^4 m^{-3} kg^{-1}
ϵ_{RF} [a]	71
V [b]	54.0 nm^3
$\frac{\langle \Delta V^2\rangle}{\langle V\rangle}$ [b]	9.93×10^{-4} nm^3
$\langle \mathbf{M}^2\rangle - \langle \mathbf{M}\rangle^2$ [b]	14 367 D^2
P [b]	0.0359 C m^{-2}
β [c]	2.32×10^{-10} Pa^{-1}
ϵ [c]	32.8
$\frac{\partial P}{\partial p}$ [c]	96.6 pC N^{-1}

[a] Known or selected constants and properties.
[b] Found directly from MD.
[c] Calculated using theory with values from MD.

5.1. Compressibility of tropoelastin

For an NPT ensemble as we have used here, the isothermal compressibility can be found from a statistical formula relating the fluctuations of the volume around a mean

value [31].

$$\beta = \frac{1}{k_b T} \frac{\langle \triangle V^2 \rangle}{\langle V \rangle}. \tag{20}$$

To find the volume fluctuations of the protein, we follow a similar algorithm as that used by Dadarlat and Post [32]. In this method we form a three dimensional grid around the protein to form a mesh of small cubes. Then we check to see if the cube is located within the Van der Waals radius of any atom in the protein. If true, the volume of the cube is added to the volume of the protein, otherwise the cube is regarded as empty. This is performed over a volume encompassing the entire protein, and the volume of all cubes meeting the criteria described is summed to estimate the volume of the protein.

A spacing of 0.2 nm between grid points was used, and this gives each cube formed by the grid a volume slightly lower than that of a sphere formed using the average Van der Waals radius of the atoms in the tropoelastin protein. The method of Dadarlat and Post also includes a "Van der Waals expansion coefficient", γ, in order to include free space inside the protein not accessible to solvent molecules in the protein's volume. We include this parameter in our calculations with the same value, $\gamma = 1.3$, by simply multiplying the Van der Waals radii by the expansion coefficient.

Taking the coordinates of the atoms at 2 ps intervals over a 1 ns simulation yields 500 data points to use for the time averaged volume and volume fluctuations. The mean volume over 1 ns is found to be 54.0 ± 0.23 nm^3. The volume is verified using the program MSMS which calculates the solvent accessible surface and volume of a molecule [33]. Since we are only interested in the volume, we choose a small probe radius of 0.001 nm rather than the default of 0.15 nm which overestimates the volume. This method gives a value of 53.606 nm^3 for the single configuration of the tropoelastin molecule tested which agrees well with the value that we predict.

Finally, using, Eq. (20) we estimate the compressibility to be 2.32×10^{-10} Pa^{-1}. This is similar in magnitude to the compressibilities of other proteins calculated in a likewise manner [32].

5.2. Dielectric constant of tropoelastin

In a similar vein, the relative dielectric constant ϵ can also be found from molecular dynamics by monitoring the fluctuations of the protein's dipole moment. Following the Frohlich–Kirkwood theory [34], we have

$$\epsilon = \frac{1 + \frac{\langle \mathbf{M}^2 \rangle - \langle \mathbf{M} \rangle^2}{3\epsilon_0 V k_b T} \frac{2\epsilon_{RF}}{(2\epsilon_{RF}+1)}}{1 - \frac{\langle \mathbf{M}^2 \rangle - \langle \mathbf{M} \rangle^2}{3\epsilon_0 V k_b T} \frac{1}{(2\epsilon_{RF}+1)}}. \tag{21}$$

Although this equation appears complex, most of the values are known or are very straight forward to obtain from molecular dynamics. The other variable in (21) is the relative dielectric permittivity of the reaction field, ϵ_{RF}; for our simulations we use SPC/E water molecules as the solvent and therefore choose $\epsilon_{RF} = 71$ [35]. However, in simulations for up to only 1 ns, as we have done so far, the value of the dipole fluctuations may vary greatly for different simulations. Therefore, results were taken from simulations started from four slightly different configurations, and run until the time averages of the dipole fluctuations converged. The four simulations converge on the same value of the fluctuations after running for 10 ns of simulation time. Finally, using this result with Eq. (21) yielded a relative dielectric constant of $\epsilon = 32.8$ for tropoelastin. This value is in line with the higher end of the range of dielectric constants calculated for many other proteins [34].

5.3. Piezoelectric coefficient

Recall that the spontaneous polarization, P, for tropoelastin found earlier is 3.59 μC cm^{-2}. Using this along with the values found for the compressibility, β, and the dielectric constant of tropoelastin, ϵ, the piezoelectric coefficient given by (19) can be computed. With the properties highlighted in Table 1, we find the piezoelectric coefficient for tropoelastin to be 96.6 pC N^{-1}, a very reasonable result when compared with other piezoelectric polymers. For example PVDF polymers have been shown to have piezoelectric coefficients with magnitudes as high as 33 pC N^{-1} [36], and lead zirconate titanate (PZT), a ceramic, has reported coefficients as high as 584 pC N^{-1} [37]. So far we have made no mention of the tensorial aspect of the piezoelectric response. Therefore the calculated coefficient presented here should be taken to be when the stress is applied in the same direction as the dipole.

What we have found here is the piezoelectric coefficient for a single tropoelastin monomer. The more easily measurable value would be the coefficient of a bulk elastin sample. Just as the polarization for the bulk elastin found experimentally was lower than the calculated polarization for a single monomer, we expect a similar result for the piezoelectric coefficient. As a crude first approximation of the piezoelectric coefficient for bulk elastin, we use the fact that the actual polarization was 56% of the single monomer value. Since Eq. (19) shows that the piezoelectric coefficient scales linearly with the polarization, the piezoelectric coefficient of elastin can be estimated as 56% of the value found for tropoelastin. This argument then puts the piezoelectric coefficient of elastin to be 53.8 pC N^{-1}. As expected, this estimate is too crude and only puts the results within an order of magnitude of the thin-film measured results [9]—indeed, upscaling from a single tropoelastin monomer to a thin film is a non-trivial task and beyond the scope of the present manuscript.

6. Discussion

In this work, the mechanism underpinning biological ferroelectricity has been elucidated through the combined use of statistical mechanics, molecular dynamics, and insights from experimental results. Our model is fairly simple and allows a facile calculation of several properties that are not easily estimated from experiments e.g. piezoelectricity.

At first glance it may seem that the proposed switching mechanism and model are not specific to elastin and its tropoelastin precursor. Elastin is only the first biological material shown to exhibit ferroelectric behavior; there may well be others, some of which may even share the same switching mechanism as elastin. The uniqueness of the switching mechanism presented here lies in the properties of the material itself. First, elastin is a relatively soft protein. This characteristic is what makes elastin such an integral part of our organ's elastic response to any deformations. Other proteins may be too stiff to undergo the same deformation as elastin/tropoelastin under a similar electric field and would therefore show no signs of ferroelectricity (or the response will be weak enough to be impractical). The unstructured and asymmetrical nature of tropoelastin also plays a role. Many proteins exist as oligomers or other structures that exhibit higher symmetry, compared to a tropoelastin monomer or essentially amorphous elastin polymer. The lack of lower symmetry could prevent general proteins the necessary properties such as a dipole moment or cross-linking required for the proposed switching mechanism.

A key open question involves determining the physiological role of ferroelectricity—something that is beyond the scope of this short communication. As mentioned earlier, experimental results have shown that in glucose treated samples of elastin the ferroelectric response is suppressed or even completely eliminated [9]. Since glucose will naturally build up in extracellular elastin as we age, due to glycation, it is believed that ferroelectricity may be intimately linked with the aging process. An intriguing future direction is to modify the model developed in this communication to account for glycation. Knowing the mechanism by which biological ferroelectricity occurs, we may speculate on some possible reasons for the loss of ferroelectricity in elastin due to the build up of glucose. For one, the glucose may alter the dipole moment of tropoelastin; for example, additional glucose could reduce or negate the dipole moment which would clearly lead to a reduction in the ferroelectric response of elastin. Another possibility is that as glucose binds to the tropoelastin monomers, it causes a shift in the band gap changing the elastin from an insulator to a conductor which would not exhibit any ferroelectric behavior. Perhaps the most likely possibility, is that as glucose binds to the elastin/tropoelastin, there is an increase in intermolecular cross-links between elastin chains. This would prevent the tropoelastin molecules from rotating or deforming as freely under the application of an electric field, thus damping out the ferroelectric behavior as more cross-links are formed.

Ferroelectric materials are also known to be both piezoelectric and pyroelectric. We have made the first attempt to find the piezoelectric coefficient for elastin. This is, as yet, an experimentally untested prediction.

Acknowledgments

We gratefully acknowledge support from the NSF GK12 Program and NSF CMMI 1463205.

References

[1] E. Fukada, I. Yasuda, On the piezoelectric effect of bone, J. Phys. Soc. Japan 12 (1957) 1158–1162.
[2] S.B. Lang, Pyroelectric effect in bone and tendon, Nature 212 (1966) 704–705.
[3] Y. Liu, Y. Zhang, M. Chow, Q.N. Chen, J. Li, Biological ferroelectricity uncovered in aortic walls by piezoresponse force microscopy, Phys. Rev. Lett. 108 (2012) 078103.
[4] L. Debelle, A.M. Tamburro, Elastin: molecular descriptor and function, Int. J. Biochem. Cell Biol. 31 (1999) 261–272.
[5] A. Ostuni, B. Bochicchio, M.F. Armentano, F. Bisaccia, A.M. Tamburro, Molecular and supramolecular structural studies on human tropoelastin sequences, Biophys. J. 93 (2007) 3640–3651.
[6] Z. Indik, K. Yoon, S.D. Morrow, G. Cicila, J. Rosenbloom, J. Rosenbloom, N. Ornstein-Goldstein, Structure of the 3' region of the human elastin gene: great abundance of alu repetitive sequences and few coding sequences, Connect. Tissue Res. 16 (1987) 197–211.
[7] C. Baldock, A.F. Oberhauser, L. Ma, D. Lammie, V. Siegler, S.M. Mithieux, Y. Tu, J.Y.H. Chow, F. Suleman, M. Malfois, S. Rogers, L. Guo, T.C. Irving, T.J. Wess, A.S. Weiss, Shape of tropoelastin, the highly extensible protein that controls human tissue elasticity, PNAS 108 (2011) 4322–4327.
[8] G. Faury, Function-structure relationship of elastic arteries in evolution: from microfibrils to elastin and elastic fibres, Pathol. Biol. 49 (2001) 310–325.
[9] Y. Liu, Y. Wang, M. Chow, N. Chen, F. Ma, Y. Zhang, J. Li, Glucose suppresses biological ferroelectricity in aortic elastin, Phys. Rev. Lett. 110 (2013) 168101.
[10] A.J. Bailey, Molecular mechanisms of ageing in connective tissues, Mech. Ageing Dev. 122 (2001) 735–755.
[11] F.W. Danby, Nutrition and ageing skin: sugar and glycation, Clin. Dermatol. 28 (2010) 409–411.
[12] M.J. Sherratt, Tissue elasticity and the ageing elastic fibre, AGE 31 (2009) 305–325.
[13] M. Brownlee, Advanced protein glycosylation in diabetes and ageing, Annu. Rev. Med. 46 (1995) 223–234.
[14] M.G. Broadhurst, G.T. Davis, Ferroelectric polarization in polymers, Ferroelectrics 32 (1981) 177–180.
[15] U. Pieper, B.M. Webb, D.T. Barkan, D. Schneidman-Duhovny, A. Schlessinger, H. Braberg, Z. Yang, E.C. Meng, E.F. Pettersen, C.C. Huang, R.S. Datta, P. Sampathkumar, M.S. Madhusudhan, K. Sjolander, T.E. Ferrin, S.K. Burley, A. Sali, Modbase, a database of annotated comparative protein structure models, and associated resources, Nucleic Acids Res. 39 (2011) D465–D474.
[16] CATH version 3.5 release notes, 2013. http://www.cathdb.info/wiki/doku/?id=release_notes.
[17] Y. Yang, E. Faraggi, H. Zhao, Y. Zhou, Improving protein fold recognition and template-based modeling by employing probabilistic-based matching between predicted one-dimensional structural properties of query and corresponding native properties of templates, Bioinformatics 27 (2011) 2076–2082.
[18] H. Bekker, H.J.C. Berendsen, E.J. Dijkstra, S. Achterop, R. van Drunen, D. van der Spoel, A. Sijbers, H. Keegstra, B. Reitsma, M.K.R. Renardus, Gromacs: A parallel computer for molecular dynamics simulations, Phys. Comput. 92 (1993).
[19] H.J.C. Berendsen, D. van der Spoel, R. van Drunen, Gromacs: A message-passing parallel molecular dynamics implementation, Comput. Phys. Comm. 91 (1995) 43–56.
[20] E. Lindahl, B. Hess, D. van der Spoel, Gromacs 3.0: A package for molecular simulation and trajectory analysis, J. Mol. Model. 7 (2001) 306–317.
[21] D. van der Spoel, E. Lindahl, B. Hess, G. Groenhof, A.E. Mark, H.J.C. Berendsen, Gromacs: Fast, flexible, and free, J. Comput. Chem. 26 (2005) 1701–1718.
[22] B. Hess, C. Kutzner, D. van der Spoel, E. Lindahl, Gromacs 4: Algorithms for highly efficient, load-balanced, adn scalable molecular simulation, J. Chem. Theory Comput. 4 (2008) 435–447.
[23] A.D. MacKerell, D. Bashford, Bellott, R.L. Dunbrack, J.D. Evanseck, M.J. Field, S. Fischer, J. Gao, H. Guo, S. Ha, D. Joseph-McCarthy, L. Kuchnir, K. Kuczera, F.T.K. Lau, C. Mattos, S. Michnick, T. Ngo, D.T. Nguyen, B. Prodhom, W.E. Reiher, B. Roux, M. Schlenkrich, J.C. Smith, R. Stote, J. Straub, M. Watanabe, J. Wirkiewicz-Kuczera, D. Yin, M. Karplus, All-atom empirical potential for molecular modeling and dynamics studies of proteins, J. Phys. Chem. B 102 (1998) 3586–3616.
[24] W. Humphrey, A. Dalke, K. Schulten, VMD—visual molecular dynamics, J. Mol. Graph. 14 (1996) 33–38.
[25] A.M. Tamburro, B. Bochicchio, A. Pepe, Dissection of human tropoelastin: Exon-by-exon chemical synthesis and related conformational studies, Biochemistry 42 (2003) 13347–13362.

[26] P. Brown-Augsburger, C. Tisdale, T. Broekelmann, C. Sloan, R.P. Mecham, Identification of an elastin crosslinking domain that joins three peptide chains, possible role in nucleated assembly, J. Biol. Chem. 270 (1995) 17778–17783.
[27] Y. Liu, H.L. Cai, M. Zelisko, Y. Wang, J. Sun, F. Yan, F. Ma, P. Wang, Q.N. Chen, H. Zheng, X. Meng, P. Sharma, Y. Zhang, J. Li, Ferroelectric switching of elastin, Proc. Natl. Acad. Sci. 111 (2014) E2780–E2786.
[28] R.B. Olsen, J.C. Hicks, M.G. Broadhurst, G.T. Davis, Temperature-dependent ferroelectric hysteresis study in polyvinylidene fluoride, Appl. Phys. Lett. 43 (1) (1983) 127–129.
[29] D. Kroshko, OpenOpt: Free scientific-engineering software for mathematical modeling and optimization, 2007. http://www.openopt.org/.
[30] F.I. Mopsik, M.G. Broadhurst, Molecular dipole electrets, J. Appl. Phys. 46 (1975) 4204–4208.
[31] T.L. Hill, An Introduction to Statistical Thermodynamics, Volume, Addison-Wesley, 1960, pp. 37–38. (Chapter 2).
[32] V.M. Dadarlat, C.B. Post, Insights into protein compressibility from molecular dynamics simulations, J. Phys. Chem. 105 (2001) 715–724.
[33] M.F. Sanner, A.J. Olson, J.C. Spehner, Reduced surface: An efficient way to compute molecular surfaces, Biopolymers 38 (1996) 305–320.
[34] J.W. Pitera, M. Falta, W.F. van Gunsteren, Dielectric properties of proteins from simulation: The effects of solvent, ligands, ph, and temperature, Biophys. J. 80 (2001) 2546–2555.
[35] M.R. Reddy, M. Berkowitz, The dielectric constant of SPC/E water, Chem. Phys. Lett. 155 (1989) 173–176.
[36] E.L. Nix, I.M. Ward, The measurement of the shear piezoelectric coefficients of polyvinylidene flouride, Ferroelectrics 67 (1986) 137–141.
[37] Q. Guo, G.Z. Cao, I.Y. Shen, Measurements of piezoelectric coefficient d_{33} of lead zirconate titanate thin films using a mini force hammer, J. Vib. Acoust. 135 (2013) 011003.